An enhanced photo(electro)catalytic CO_2 reduction onto advanced BiOX (X = Cl, Br, I) semiconductors and the BiOI–PdCu composite

J. Manuel Mora-Hernandez [a,*], Luis A. Alfonso Herrera [b], Luis F. Garay-Rodriguez [b], Leticia M. Torres-Martínez [b,c], Irina Hernandez-Perez [b]

[a] CONAHCYT - Universidad Autónoma de Nuevo León, UANL, Facultad de Ingeniería Civil, Departamento de Ecomateriales y Energía, Av. Universidad S/N Ciudad Universitaria, San Nicolás de los Garza, Nuevo León, C.P. 66455, Mexico
[b] Universidad Autónoma de Nuevo León, UANL, Facultad de Ingeniería Civil, Departamento de Ecomateriales y Energía, Av. Universidad S/N Ciudad Universitaria, San Nicolás de los Garza, Nuevo León, C.P. 66455, Mexico
[c] Centro de Investigación en Materiales Avanzados, S.C. (CIMAV), Miguel de Cervantes No. 120. Complejo Ind. Chihuahua, Chihuahua, Chih, C.P. 31136, Mexico

ARTICLE INFO

ABSTRACT

The photoelectrocatalytic reduction of CO_2 (CO_2RR) onto bismuth oxyhalides (BiOX, X = Cl, Br, I) was studied through physicochemical and photoelectrochemical measurements. The successful synthesis of the BiOX compounds was carried out through a solvothermal methodology and confirmed by XRD measurements. The morphology was analyzed by SEM; meanwhile, area and pore size were determined through BET area measurements. BiOI and BiOCl present a lower particle size (3.15 and 2.71 μm, respectively); however, the sponge-like morphology presented by BiOI results in an increase in the BET area, which can enhance the catalytic activity of this semiconductor. In addition, DRS measurements allowed us to determine bandgap values of 1.9, 2.4, and 3.6 eV for BiOI, BiOBr, and BiOCl, respectively. Such results predict better visible light harvesting for BiOI. Photoelectrochemical measurements indicated that BiOX shows p-type semiconductor behavior, being the holes the majority charge carriers, making BiOI the most active material to carry out photoelectrocatalytic CO_2RR. In the second stage, three different composites, BiOI–Pd, BiOI–Cu, and BiOI–PdCu, (BiOI-M; M = Pd, Cu, PdCu), were fabricated to study the influence of active metal nanoparticles (NP's) in the BiOI CO_2RR activity. XRD measurements confirmed the interaction between BiOI and the metallic NP's, the three composites overpassed by 20% the BET area of pristine BiOI. Photoelectrochemical measurements indicate that all BiOI-metal composites are suitable materials to perform CO_2 reduction in neutral media efficiently; however, the BiOI–PdCu composites surpassed the faradaic current of BiOI–Pd and BiOI–Cu at 0.85 V vs. RHE (3.15, 2.06 and 2.15 mA cm^{-2}, respectively). BiOI–PdCu presented photoactivity to carry out the CO_2 reduction evolving formic acid and acetic acid as the main products under visible-light irradiation.

* Corresponding author. Av. Universidad and Av. Fidel Velázquez S/N, Cd. Universitaria, San Nicolás de los Garza, Nuevo León, C.P. 66455, Mexico.
E-mail addresses: jmorah@conacyt.mx, jmmora@live.com.mx (J.M. Mora-Hernandez).

1. Introduction

In the last two decades, global warming and climate change have become common terms used in social, technical, and scientific communications to relate the damage caused to the environment and climatic disasters by non-sustainable human activities [1,2]. As an indicator of global warming potential, the carbon footprint (CF) is used as a quantitative statement to measure and quantify the greenhouse gases (GHG) emissions, including the accumulation of CO_2, CH_4, and NO_X emissions [3]. Based on data from the Organization for Economic Co-operation and Development, the International Energy Agency, and the Solar Heating & Cooling Program (OECD/IEA and IEA SHC), the combustion of fossil fuels produced 80% of the total global energy consumption. Nevertheless, these combustion processes release many toxic compounds into the atmosphere (CO_2, CO, NO_X, and SO_X), making CO_2 the second most abundant greenhouse gas, only below water vapor [4–7]. Several negative impacts are projected for a global warming rise of 2 °C relative to pre-industrial levels for particularly vulnerable geographical regions; many countries advocate limiting global warming to below 1.5 °C by 2100 [8]. This goal could be achieved through an earlier transition to net zero carbon emissions in 2060 [9]; in this context, several research groups have invested many efforts to mitigate the excessive use of fossil fuels in energy generation to cover the global demand [10–12].

Photoelectrocatalysis (PEC) is an emerging but promising technology with several applications in environmental remediation; it takes advantage of electrochemical fundamentals strengthened by photochemical processes, thus promoting an enhanced charge transport capable of performing peculiar redox reactions. Since PEC requires low temperature and considerable pressure conditions, it has gained attention; however, PEC technology bases its operation on developing efficient photoelectrocatalytic materials. Several photoactive materials have been evaluated for energy generation and environmental remediation. Regarding CO_2 reduction, TiO_2-based materials have shown promising efficiency; in 2021, Liu et al. studied the modification of InP photocathodes with Au–TiO_2 to understand the interface's role in performing the PEC CO_2 reduction. The authors conclude that the InP nanostructure promoted light harvesting, thus increasing the charge carrier's lifetime and decreasing the recombination rate. In addition, the InP photocathodes promote a high selectivity towards CO formation due to the different contact points between Au and TiO_2. Theoretical studies suggest that Au transfers electrons to TiO_2 in a confined environment, which produces a deficiency of electrons in Au, increasing its affinity towards the intermediate species CO*, thus explaining its selectivity towards CO production. The optimized material Au–TiO_2/InP presented an onset potential of +0.3 V vs. RHE, resulting in a Faradaic efficiency of 84.2% for CO generation at −0.11 V vs. RHE using a simulated AM 1.5G illumination at one sun [13]. Merino Garcia et al. synthesized TiO_2 nanoparticles (NP's) using a supercritical medium (SC) of CO_2 at 20 MPa and 300 °C; they deposited TiO_2 NP's synthesized under these conditions (SC–TiO_2) in a porous carbon paper. SC-TiO_2 showed enhanced optical properties, surface area, crystallinity, and overpassing TiO_2–P25 towards the PEC production of ethylene and methanol, thus indicating that a supercritical medium is an effective strategy to synthesize materials with high efficiency towards PEC CO_2 reduction [14].

In 2022, Li et al. synthesized a heterostructure of Si wafer - TiO_2 layer - Sn metal particles through hydrothermal and electrodeposition methods. Due to Sn metal's surface plasmon resonance effect, the heterostructure Si/TiO2/Sn showed enhanced optical properties. Additionally, the heterostructure presented high faradaic efficiency and selectivity to reduce CO_2 to HCOOH, generating 4.72 mA cm^{-2} at −1.0 V vs. RHE. Si/TiO2/Sn's faradaic efficiency remains above 60% after 8 h, indicating high stability [15].

Other novel inorganic, organic, and hybrid materials have shown interesting PEC activity toward CO_2 reduction. In 2019, Wang et al. studied the selective PEC CO_2 reduction to CO using the halide-organic perovskite $CH_3NH_3PbBr_3$ coupled with graphene oxide, obtaining high selectivity and excellent faradaic efficiency [16]. In 2020, Wang et al. studied covalent organic frameworks for PEC CO_2 reduction; in this work, the Cu@porphyrin-COF effectively produced ethanol, methanol, acetone, 1-diol, and ethane-1 [17]. In 2021, Xu et al. developed a bio-cathode FDH(enzyme)/g-C_3N_4 combined with the photoanode Ta_3N_5. This PEC system produced a selective and efficient PEC CO_2 reduction to produce formate [18]. Similarly, Zhou et al. studied the selective CO_2 reduction to CO or alcohols using the photocathode Cu_2ZnSnS_4(CZTS)/CdS; the authors conclude that oxygen vacancies are useful for promoting the selective formation of a specific desirable product [19]. Finally, in 2022, Ren et al. coupled metallic sulfides with metal-organic frameworks to develop the composite Bi_2S_3/ZIF-8, which presented an efficient and selective CO_2 reduction to formate [20].

Recently, bismuth oxyhalides (BiOX; X = F, Cl, Br, I, At) have sparked the scientific community's interest since BiOX are economical and efficient photocatalysts [21]. BiOX materials present a tetragonal matlockite structure consisting of BiO_2 layers inserted into double halogen layers [21]. Such a peculiar structure can promote the polarization of the BiO_2 and halogens layers producing an electric field capable of inducing an efficient charge separation and transport, which are crucial properties in PEC reactions [21]. Regarding optical properties, computational experiments indicate that BiOCl, BiOBr, and BiOI bandgap are 2.5, 2.1, and 1.6 eV, respectively. The density of states analysis shows that the 2p orbitals of oxygen atoms and np orbitals of halogens (n = 3, 4, and 5 for X = Cl, Br, and I, respectively) compose the top of the valence band. In contrast, the 6p orbitals of Bi compose the conduction band [22]. BiOX materials present an indirect bandgap, meaning that the photo-induced electrons in the conduction band are separated from the valence band for a certain k-distance, which reduces the recombination rate [21]. The bandgap of BiOX materials decreases when the atomic number of the halogen atoms increases due to halogens lower in the periodic table presenting p orbitals closer in energy with 6p orbitals of Bi, resulting in an effective overlap. In this way, BiOI (I 5p) presents the narrowest bandgap, converting it into an interesting photoelectrocatalytic material with activity under visible light. Nevertheless, BiOI also shows the highest inherent recombination rate among the BiOX materials [21]; therefore, developing strategies that improve charge separation in BiOI is crucial to producing an efficient PEC system based on such material.

A practical strategy to diminish the recombination rate is the metal NP's deposition on the photoelectrocatalyst's surface since metal NP's can act as an electron acceptor, promoting charge transference [23]. The deposition of Pd^0 NP's has been an effective strategy to enhance the PEC activity of Bi materials such as $BiVO_4$ [24] or BiOBr [25]. In addition, Pd or Cu NP's can induce energetic

states in the co-catalyst interface, resulting in a modification of their band structure and a lower recombination rate [26]. It suggests that Pd and Cu materials can present synergetic properties for PEC applications; indeed, in 2021, Zhang et al. demonstrated that the composite Pd/CuO presents an irreversible electronic transference from CuO to Pd associated with the Schottky barrier that improves charge mobility and reduces the recombination rate [27]. Consequently, it is proposed that composites Pd–Cu_2O present synergistic features capable of boosting the charge mobility of the photoactive BiOI, reducing its limitations as an active phase in PEC systems.

This work aims to elucidate the electro- and photo-catalytic properties of three bismuth oxyhalides, BiOCl, BiOBr, and BiOI, determining their physicochemical and photoelectrocatalytic features that make them active photocatalysts to carry out the PEC CO_2 reduction and establishing the parameters that make BiOI the most active photoelectrocatalyst. In the second stage, the PEC activity of three composites based on the BiOI semiconductor doped with Pd, Cu, and PdCu NP's was evaluated. The physicochemical properties of the new composites and their interaction between the semiconductor and metallic NP's improved their performance towards the PEC CO_2 reduction.

2. Materials and methods

2.1. Synthesis of BiOX (X = Cl, Br, I) photocatalysts

The BiOX (X = Cl, Br, I) photocatalysts were prepared through a solvothermal method, mixing 1 mmol of bismuth nitrate (Bi $(NO_3)_3 \cdot 5H_2O$, 99.99%, Sigma Aldrich), 10 ml of ethylene glycol and 1 mmol of a potassium halide as precursor: KCl (99.9% DEQ), KBr (99% Sigma Aldrich) or KI (99.3%, FERMONT). The solution was placed into a solvothermal reactor consisting of a Teflon reactor inside an inox steel reactor which was sealed and heated until 160 °C for 12h. At the end of the heating process, the reaction products were rinsed first three times with ethanol, then rinsed with water three times. Each rinse employs 6 ml of ethanol or water to avoid the presence of ethylene glycol in the final samples (Fig. S1). The samples were finally dried 8 h at 60 °C under an air atmosphere. The resulting powders were stored for physicochemical characterizations.

2.2. Synthesis of Pd NP's

Palladium NP's were obtained through an aqueous chemical reduction process, and palladium chloride ($PdCl_2$, 99%, Sigma-Aldrich) was used as the Pd precursor. The procedure involves the dissolution of $PdCl_2$ (83 mg) in ultra-pure water (30 ml); then, polyvinylpyrrolidone (140 mg) (PVP10, Sigma-Aldrich) was added to the previous mix (solution 1). Solution 2 containing sodium borohydride (267 mg) ($NaBH_4$ 99.99% Sigma-Aldrich) in distilled water (20 ml) was added to solution 1; this third solution was stirred for 6 h at room temperature and then filtered. The metal powders obtained were mixed with Vulcan carbon XC-72 (200 mg), distilled water (20 mL), and isopropanol (5 mL). The resulting solution was stirred for 12 h at 25 °C and dried at 90 °C.

2.3. Synthesis of Cu NP's

The synthesis of copper NP's was achieved by mixing ethylene glycol (5 ml) ($C_2H_6O_2$, 99.8 Fermont) and ascorbic acid (693 mg) ($C_6H_8O_6$, 99%, Sigma-Aldrich) (solution 1). A second solution containing PVP (236 mg) dissolved in $C_2H_6O_2$ (20 mL) was mixed with solution 1. After stirring and heating for 15 min at 60 °C, copper acetate (157 mg) ($Cu(CH_3COO)_2 \cdot H_2O$, 99.2% Fermont) was added to this third solution. The final mixture was stirred 4 h at 60 °C; the metal powders were washed and mixed with Vulcan carbon XC-72 (200 mg), distilled water (20 mL), and isopropanol (5 mL). The resulting solution was stirred for 12 h at 25 °C and dried at 90 °C.

2.4. Synthesis of PdCu NP's

For synthesizing the bimetallic PdCu (1:1 wt% ratio), deionized water (30 ml) and $PdCl_2$ (41.3 mg) were mixed and stirred for 15 min. $Cu(CH_3COO)_2 \cdot H_2O$ (78.5 mg) was added to the first solution; after 15 min stirring PVP (140 mg) was added (solution 1). Solution 2, containing sodium borohydride (266.6 mg) in ultra-pure water (20 ml) was mixed with solution 1. After 6 h stirring, the metal powders were washed and mixed with Vulcan carbon XC-72 (200 mg), distilled water (20 mL), and isopropanol (5 mL). The resulting solution was stirred for 12 h at 25 °C and dried at 90 °C.

2.5. Preparation of the photoelectrocatalysts

The three photoelectrocatalysts, BiOI-M (M = Pd, Cu, PdCu), were prepared following a wet impregnation method. In short, 5 mg of the metal powder and 5 mg of BiOI were used to prepare a solution by adding 5 ml of isopropanol and 20 ml of water. The solution was stirred for 12 h at 25 °C, and then dried at 90 °C. The resulting powders were carefully ground in a mortar to prepare a catalytic ink; mixing 10 mg of the catalytic powder, 125 μl of Nafion® (5 wt%), 1250 μl of ultra-pure water (18 MΩ cm), and 125 μl of ethanol. The resulting ink was stirred for 20 min.

2.6. Preparation of electrodes

To perform the electrocatalytic tests, the materials were electrochemically evaluated by depositing 3 μl of the catalytic ink onto a glassy carbon (GC) electrode (3 mm diameter). To carry out the photo(electro)catalytic tests, 10 μl of the catalytic ink were deposited

by spin coating onto conductive ITO glass. The photocatalytic surface area of the working electrode was 1 cm^2. The electrodes were dried under N_2 prior to the electrochemical tests.

2.7. Instrumentation

X-ray diffraction (XRD) measurements were performed using a Bruker D8 device operating at 40 kV and 40 mA, employing CuK radiation (λ = 1.5406 Å). The step size was 0.05° and the counting time 0.05 s per step in a 2θ range from 10° to 70°. The materials morphology was observed using a scanning electron microscope (SEM-JEOL, 6490LV), operating in the secondary electron mode and an accelerating voltage of 20 kV. The surface area (S_{BET}) was calculated by physical nitrogen adsorption at 77 K, using a Belsorp II equipment. The materials were degassed at 25 °C for 30 min under vacuum before registering the N_2 adsorption-desorption plots. The optical properties were determined with a UV–vis NIR spectrophotometer (Cary 5000) (200–800 nm) and employing an integration sphere for diffuse reflectance measurements. The bandgap energy was obtained with the Kubelka-Munk function. An Auger Perki-nElmer PHY 560 spectrometer was used to carry out the X-ray photoelectron spectroscopy (XPS) measurements. XPS utilized an X-ray monochromatic source (Al Kα 1486.7 eV) with a 0.20 eV line width at a base pressure of ca. 4.3×10^{-10} mbar. The electrochemical measurements were performed in a potentiostat/galvanostat AUTOLAB PGSTAT302 N, using a standard three-electrodes electro-chemical cell. To conduct the photo(electro)chemical tests, a quartz photoelectrochemical cell (RRPG147 PINE-Research) was employed. The electrolyte was a N_2/CO_2 saturated 0.1 M KHCO$_3$ solution. A Pt rod was used as a counter electrode; meanwhile, an Ag/AgCl 3 M KCl was used as a reference electrode. This work's potential values are reported vs. the reference hydrogen electrode (RHE). A GC electrode (3 mm diameter) was used as the working electrode. Cyclic voltammetry (CV) and linear sweep voltammetry (LSV) were carried out at a scan rate of 50 mV s^{-1} and 20 mV s^{-1}, respectively. The photocatalytic test was carried out in a semi-batch reactor illuminated from outside with two LED lamps (λ_{max} = 420 nm), dispersing 0.1 g of the material in 200 mL of deionized water without a sacrificial agent. CO_2 gas was bubbled for 15 min to promote an anoxic media, and then, it was continuously introduced to the reactor during all the illumination time (2 h). Liquid samples were taken from the reactor (15 µL) and analyzed with an HPLC (Prominence-i, Shimadzu) equipped with a UV detector (detection at 210 nm) and an Aminex® HPX-87H column delivering 0.6 mLmin-1 of H_2SO_4 5 mM as the mobile phase at 50 °C.

3. Results and discussion

3.1. X-ray diffraction for metallic NP's and BiOX (X = Cl, Br, I)

The X-ray diffraction (XRD) measurements for the metallic NP's are presented in Fig. 1a. Pd sample shows a metal cubic phase (*Fm-3 m (225)* 01-087-0645); the signals at ca. 40.2°, 46.8°, and 68.2° correspond to the Pd° (111), (200), and (220) planes, respectively (JCPDS 46–1043). The Cu sample presents two cubic phases, cubic Cu_2O (*Pn-3 m (224)* 01-071-4310) and cubic Cu° traces (*Fm-3 m (225)* 03-065- 9743). PdCu/C does not present the XRD Cu_2O signals; however, palladium peaks are shifted to higher angles, indicating palladium to copper substitution, thus generating a PdCu solid solution [28,29]. In Table 1, it is possible to observe the cell volume distortion. Considering the theoretical unit cell of Pd, PdCu suffers the most significative cell contraction (6.29%), thus corroborating the entire solid solution formation between Cu and Pd [30,31].

The wide diffraction peaks for Pd suggest small crystallite sizes; on the other hand, the narrow peaks for Cu suggest a higher crystallization degree, thus larger crystallite sizes. Such observations were corroborated through the Scherrer equation ($d = k\lambda/B\cos\theta$),
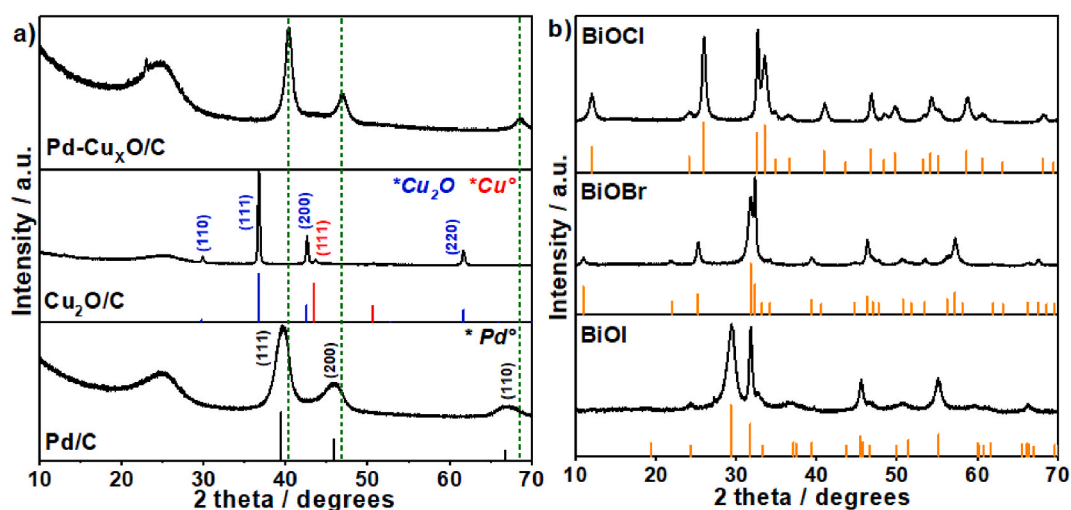

Fig. 1. X-ray diffraction patterns. a) metallic NP's, and b) BiOX (X = Cl, Br, I) semiconductors.

Table 1
XRD and S$_{BET}$ parameters.

Material	S$_{BET}$/ m^2 g^{-1}	Pore diameter/ nm	Crystallite size/nm	Lattice constant a Pd (A°)	Lattice constant a Cu$_2$O (A°)	Lattice constant a BiOI (A°)	Lattice constant c BiOI (A°)	Cell volume (A°)	Cell distortion (%)
Pd	120	12.96	9	3.9477	–	–	–	61.52	0.79*
Cu	154	13.2	62	–	4.2451	–	–	76.50	0.36§
PdCu	106	14.36	18	3.8732	–	–	–	58.10	6.26*
BiOCl	1.2	13.7	17.5	–	–	–	–	–	–
BiOBr	1.14	9.7	20.6	–	–	–	–	–	–
BiOI	5.85	18.8	23.8	–	–	3.9842	9.4066	149.32	–
BiOI–Pd	9.23	17.3	8.6	3.8989	–	3.8992	9.8297	149.44	0.9999¥
BiOI–Cu	8.65	19.9	14.8	–	4.2604	3.9744	9.4298	148.95	1.0024¥
BiOI–PdCu	8.69	19.1	16.6	3.8690	4.2168	3.9720	9.4342	148.84	1.0032¥

*Pd° Theoretical Unit Cell Volume, cubic (62.01 A°), (*Fm-3 m (225)* 01-087-0645).
§Cu$_2$O Theoretical Unit Cell Volume, cubic (76.77), (*Pn-3 m (224)* 01-071-4310).
¥BiOI Calculated Unit cell Volume, cubic (149.32), (*P4/nmm (129)* 00-010-0445).

where d is the crystallite size of the sample, k is a constant which is usually 0.9, λ is the wavelength of Cu-Kα ($\lambda = 0.154178$ nm), B is the FWHM, and θ is the Bragg diffraction angle [32]. Table 1 shows an average crystallite size of 9 nm, 62 nm, and 18 nm for Pd, Cu, and PdCu, respectively. The wide diffraction signal observed at 2θ = 25° is attributed to the Vulcan carbon used as metal support. Fig. 1b shows the XRD patterns for BiOX (X = Cl, Br, I) semiconductors. The synthesis method allows obtaining pure phases for BiOCl, BiOBr, and BiOI; they present their characteristics XRD signals corresponding to the tetragonal phases *P4/nmm (129)* 01-082-0485, *P4/nmm (129)* 01-078-0348, and *P4/nmm (129)* 00-010-0445), respectively.

3.2. Microscopy characterization

Fig. 2 shows the SEM images for BiOX (X = Cl, Br, I) semiconductors. All the materials present a spheric shape; the main difference lies in the surface morphology and particle size. BiOCl presents semi-sphere particles with the smoothest surface and an average particle size of 2.7 μm (Fig. 2c). BiOBr presents rounder particles with scales on the surface and a larger average particle size of 6.4 μm (Fig. 2b). Finally, the BiOI photocatalyst shows the most spheric morphology and the roughest surface, with an average particle size of 3.15 μm (Fig. 2a); in this way, the particle size follows BiOBr > BiOI > BiOCl. From Tables 1 and it is possible to observe that BiOX (X = Cl, Br, I) present different crystallite sizes; 17.5, 20.6, and 23.8 nm for BiOCl, BiOBr, and BiOI, respectively. It is important to consider that materials with larger crystallite sizes reduce the number of grain limits which negatively affects the charge carrier's transportation. Since BiOI presents the highest crystallization rate, this material can decrease the recombination processes, thus enhancing its photocatalytic activity [33]. Regarding roughness, it is worth mentioning that the roughest surfaces usually present a higher surface area, a desirable parameter in photoactive materials [34]. As discussed above in the XRD section, the morphological characterization by transmission electron microscopy (TEM) for the metallic Pd, Cu, and PdCu confirms the presence of well-dispersed nanoparticles (Fig. S2); such characterization was reported in a previous study [35].

3.3. DRS and BET area measurements for BiOX (X = Cl, Br, I)

The Tauc plots obtained from the UV–Vis diffuse reflectance spectroscopy (DRS) measurements for BiOX (X = Cl, Br, I) semiconductors are presented in Fig. 3a. The samples show different absorption onsets for the band transitions ranging from ∼650 to ∼300 nm. The DRS results were adjusted with the Kubelka-Munk function to correlate the band gap and to the absorption coefficient according to the equation: $(\alpha h\nu) = A (h\nu - E_g)^n$ [36,37]; α is the absorption coefficient, A is the proportionally constant, ν represents the light frequency, and E$_g$ is the band gap energy. n is related to direct (allowed), indirect (allowed), direct (forbidden), and indirect (forbidden) transitions, 1/2, 2, 3, or 3/2, respectively. In this way, according to the plot shape in Tauc plots, BiOBr and BiOCl present an indirect (allowed) transition (n = 2); meanwhile (BiOI shows a direct (allowed) transition (n = 1/2) [38]. The Eg value can be obtained by extrapolating the curve slope to the x-axis intercept; the E$_g$ values are ≈3.6, 2.4, and 1.9 eV for BiOCl, BiOBr, and BiOI, respectively [38]. Such results predict better visible light harvesting for BiOI under UV–vis irradiation.

Fig. 3b shows the adsorption-desorption isotherm for the three BiOX materials. As seen, all of them exhibit a type IV isotherm, similar to previous reports in the literature [39,40]. In this context, BiOI and BiOCl samples exhibit an H3 hysteresis loop in the pressure range of 0.7–1, implying the presence of mesopores in both materials [41]. This feature can be associated with the aggregation of smaller plate particles [42], which is more evident in the SEM image of the BiOI sample. In contrast, the BiOBr material shows an H4 hysteresis loop from 0.5 to 1 in the pressure range, associated with micropores [43]. From the adsorption isotherms, it is notorious that BiOI presents the highest adsorption volume, indicating a larger surface area (5.8 m^2 g^{-1}; Fig. 3c). This sample also exhibits the largest pore diameter (18.7 nm), resulting in a larger capacity to absorb reactive species associated with the sponge-like morphology, thus enhancing its photocatalytic activity [34].
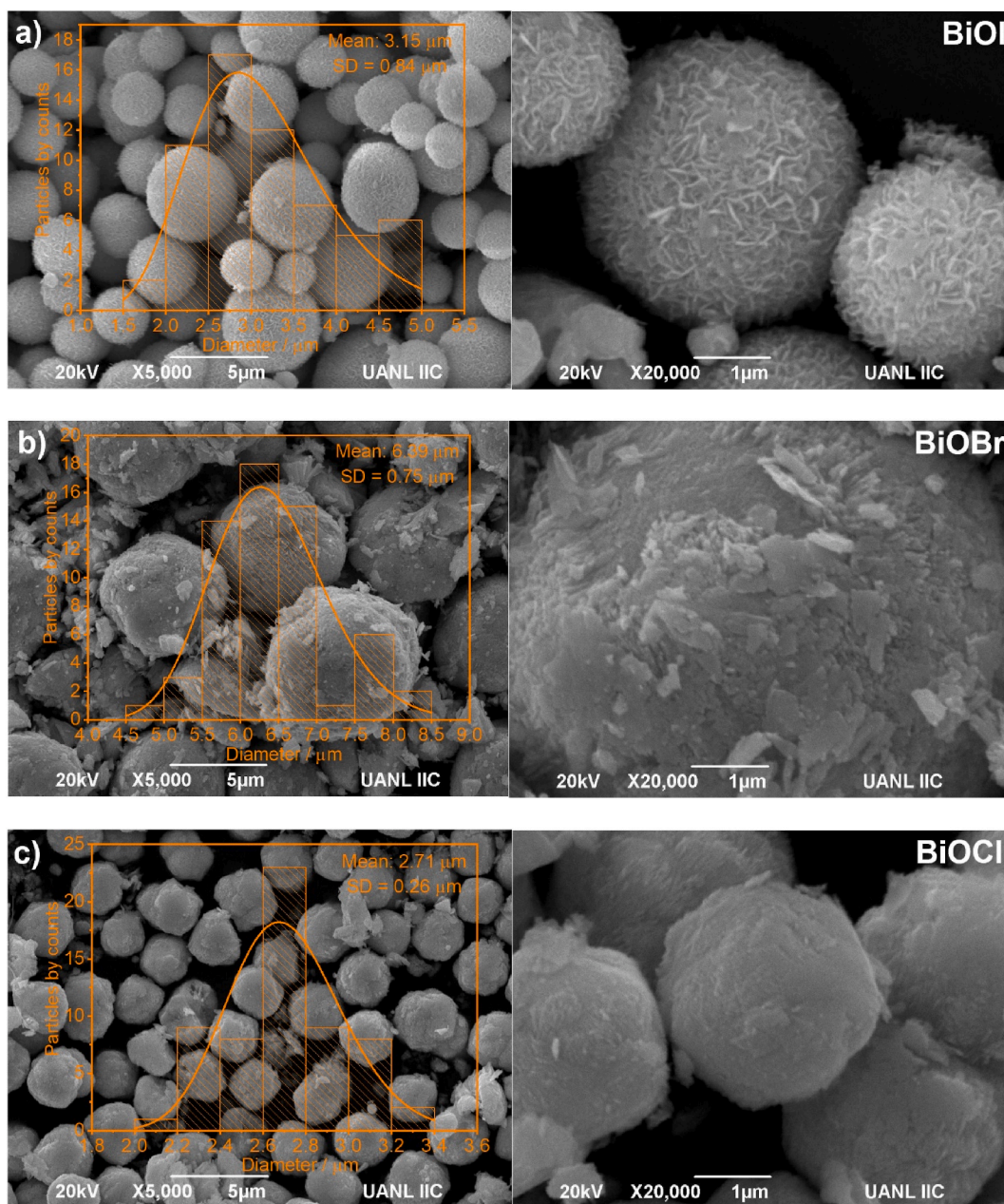
Fig. 2. Scanning electron microscopy characterization. a) BiOI, b) BiOBr, and c) BiOCl semiconductors.

3.4. Photoelectrochemical characterization for BiOX (X = Cl, Br, I)

The light-chopped open circuit potential (OCP) transients for BiOX (X = Cl, Br, I) were carried out for 300 s, lighting in the interval from 60 s to 180 s (Fig. 4a)**.** Under dark conditions, all samples show different stationary potentials related to variations in crystallinity, grain boundaries, and surface modifications [44]. Under light conditions, the photocatalytic charge carrier's generation promotes a potential displacement. The signal shifting towards higher potentials is attributed to holes accumulation on the material's surface, characteristic of a p-type semiconductor [45]. BiOCl shows the narrower potential change under light conditions, indicating instability and recombination issues [46]; on the other hand, sample BiOI presents the highest potential displacement under light conditions before reaching the steady state, indicating high activity and stability under photo-induced conditions.

The transient photocurrent measurements (Fig. 4b) were analyzed to determine the photocatalytic activity of BiOX (X = Cl, Br, I) [47]. The negative photocurrent under light conditions confirms the p-type semiconductor behavior for all the samples [48]. Since they instantly generate and eliminate the photocurrent, all the materials can be considered highly efficient under UV–Vis illumination [49].
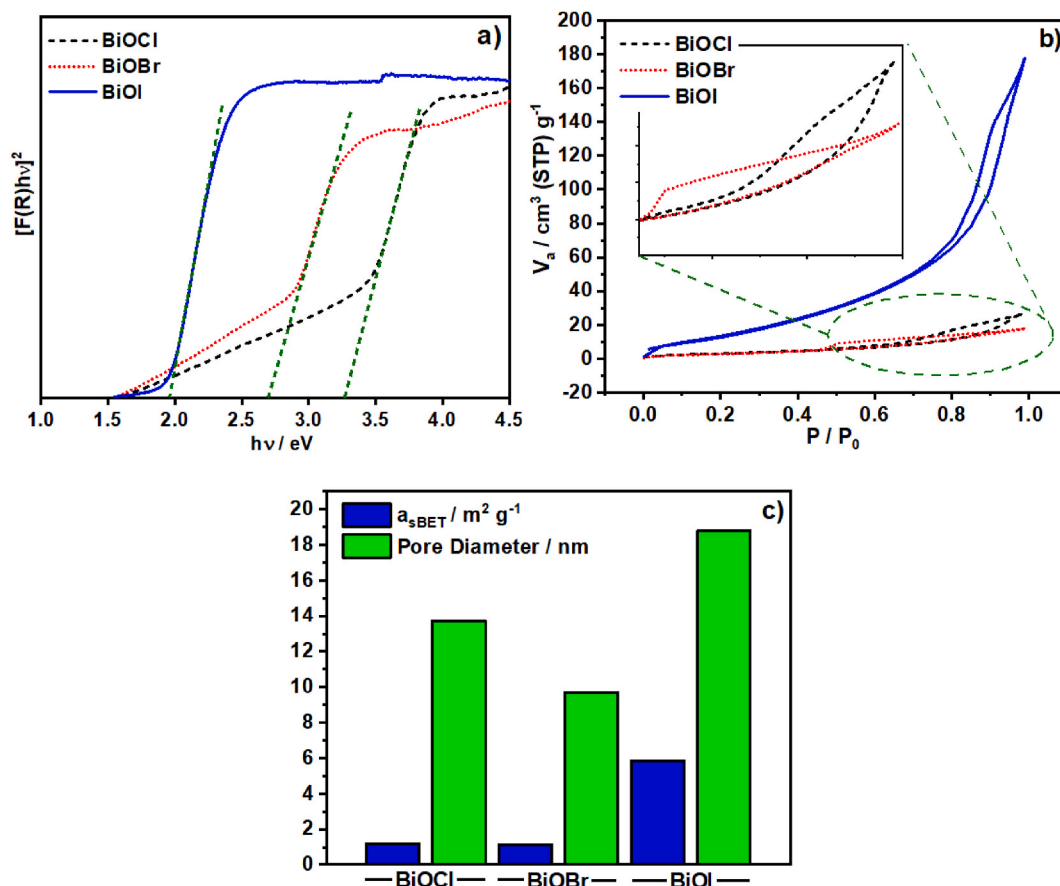
Fig. 3. a) UV–vis Diffuse Reflectance Spectra, b) Adsorption-desorption isotherms, and c) BET area and pore diameter estimations for BiOX (X = Cl, Br, I).

Regarding the photocatalytic activity, the materials follow the order; BiOI > BiOBr > BiOCl, which corroborates the results previously obtained in the OCP transients, BiOI presents the highest photocatalytic activity.

The linear sweep voltammetry (LSV) tests were performed at a scan rate of 5 mV s^{-1} under light-chopped conditions and saturating the electrolytic solution with N_2 and CO_2 atmosphere (Fig. 4c). Under a steady potential variation through reduction potential, it is possible to observe that under N_2 saturation, BiOI shows the highest photo-induced response. Additionally, BiOI achieves the lowest onset potential to carry out the hydrogen evolution reaction (HER). On the other hand, under CO_2 saturation, the onset potential decreases for all materials, indicating activity to reduce the CO_2 molecule through a photoelectrocatalytic mechanism. The onset potential follows BiOI > BiOBr > BiOCl, confirming the previous results. To corroborate the performance of the photocatalyst, Fig. 4d shows the Nyquist plots. The bias was set at −0.68 V vs. RHE to ensure appropriate conditions to perform the electrochemical impedance spectroscopy (EIS) measurements (a stationary and linear region) under CO_2 saturation conditions [50]. The semicircle presented in this plot represents the charge-transfer resistance. BiOI presented a smaller semicircle, indicating an enhanced charge transfer process at the double-layer interface. Such behavior results from an efficient charge carrier's separation and transport in the BiOI material [51]. In agreement with previous characterization methods, the EIS Nyquist plots show that BiOI presents the lowest charge transfer resistance, followed by BiOBr and BiOCl.

3.5. XRD, DRS, and BET area measurements for BiOI-M (M = Pd, Cu, PdCu)

As mentioned in section 2.5, once the BiOX (X = Cl, Br, I) were characterized and evaluated through physicochemical and electrochemical measurements, the second stage of this work consists of the formation of photoelectrocatalytic composites, consisting of most active semiconductor (BiOI) and metallic NP's to obtain the BiOI-M (M = Pd, Cu, PdCu) composites. Fig. 5a shows the XRD measurements for the three composites; the dashed black lines correspond to the BiOI tetragonal phase *P4/nmm (129)* 00-010-0445). Additionally, to the BiOI reflections, BiOI–Pd and BiOI–Cu XRD patterns show the Pd° (01-087-0645) and Cu_2O (01-071-4310) JCPDS files. On the other hand, BiOI–PdCu shows both the XRD diffraction peaks of Pd and Cu species. Such results confirm the formation of the BiOI-M (M = Pd, Cu, PdCu) composites. It is important to note that Pd peaks in BiOI–Pd present shifting to higher angles, caused by a Pd lattice contraction; Table 1 shows that the cubic lattice parameter is 3.95 for the Pd sample; however, when Pd is added to BiOI,
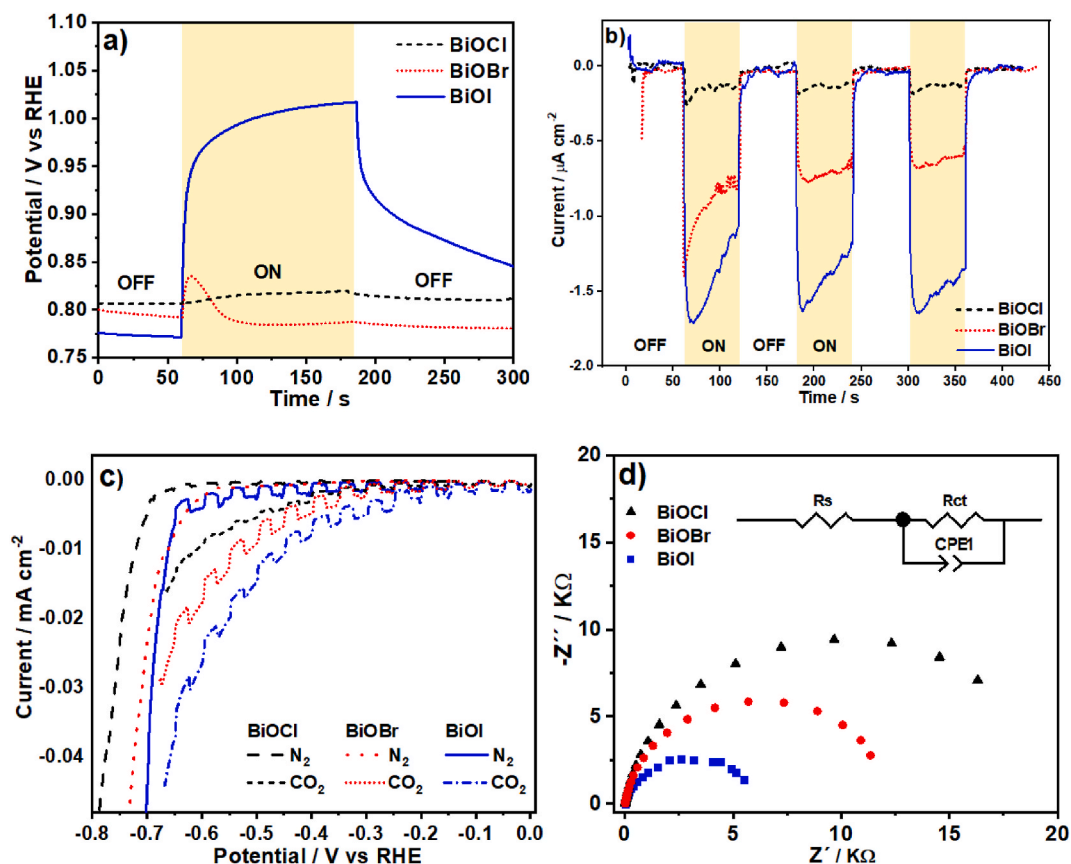
Fig. 4. a) OCP transients, b) photocurrent transients at equilibrium potential, c) LSV under cathodic polarization, and d) EIS measurements for BiOI-X (X = Cl, Br, I).

this value decreases to 3.89, thus indicating the cell contraction. Pure BiOI that initially presented a crystallite size of 23. 8 nm decreases to 8.6 in the BiOI–Pd sample; such crystallinity loss causes the widening of the BiOI XRD signals. BiOI present in BiOI–Pd also reduces their lattice parameters compared to pure BiOI, which explains the shifting to higher angles. Finally, adding Pd, Cu, or PdCu reduces the BiOI crystallite size. Incorporating these metal nanoparticles also promotes a slight lattice contraction of the lattice parameter *a*, and an enlargement of the lattice parameter *c*; the effect is more visible in sample BiOI–PdCu. In all the BIOI samples containing metal nanoparticles, the cell distortion is around 1%.

Fig. S5 shows the adsorption isotherms of the metallic nanoparticles. As seen, all of them exhibit a III-type isotherm, suggesting that those materials are non-porous. Despite this, their surface areas are larger than the ones calculated for the BiOX materials (Pd = 120 m^2 g^{-1}; Cu = 154 m^2 g^{-1}; PdCu = 106 m^2 g^{-1}), adsorbing more gas. On the other hand, Fig. 5b presents the adsorption-desorption isotherms for the three composites, where all the new materials show similar curves. Comparing the maximum volume obtained previously for bare BiOI at a relative pressure of 1.0 P_0 ($\approx$180 cm^3 (STP) g^{-1}), the new composites present an average volume close to $\approx$ 270 cm^3 (STP) g^{-1}, indicating the metal NP's incorporation allows an increase of $\approx$33% in the adsorption-desorption rate. Fig. 5c presents the a_{sBET} and pore diameter estimations; the BiOI-M (M = Pd, Cu, PdCu) composites present similar values for both measurements, although it is worth mentioning that all composites increase their surface area in comparison to bare BiOI.

3.6. Photoelectrochemical CO₂ reduction

Electrochemical (EC) and photoelectrochemical (PEC) measurements were carried out to evaluate the CO_2 reduction onto the metal NP's and BiOI (M = Pd, Cu, and PdCu) composites. The current vs. potential plots presented in Fig. 6 show four experimental conditions; i) polarization under N_2 saturation in dark conditions (black dash), ii) polarization under N_2 saturation and light irradiation (red dot), iii) polarization under CO_2 saturation in dark conditions (green dot-dash), and iv) polarization under CO_2 saturation and light irradiation (blue line).

Fig. 6a shows the cyclic voltammetry (CV) for Pd NP's; under N_2 saturation, it is possible to observe a high reduction current (−0.4 to −0.8 V vs. RHE) attributed to the electrocatalytic H_2 generation, the light induction does not produce any change since metallic Pd does not present photocatalytic activity. Under CO_2 saturation, the H_2 generation is suppressed, and a new reduction signal related to the CO_2 reduction is appreciated ($\approx$−0.25 V vs. RHE); the light irradiation does not modify the previous signal. Fig. 6c and e presents
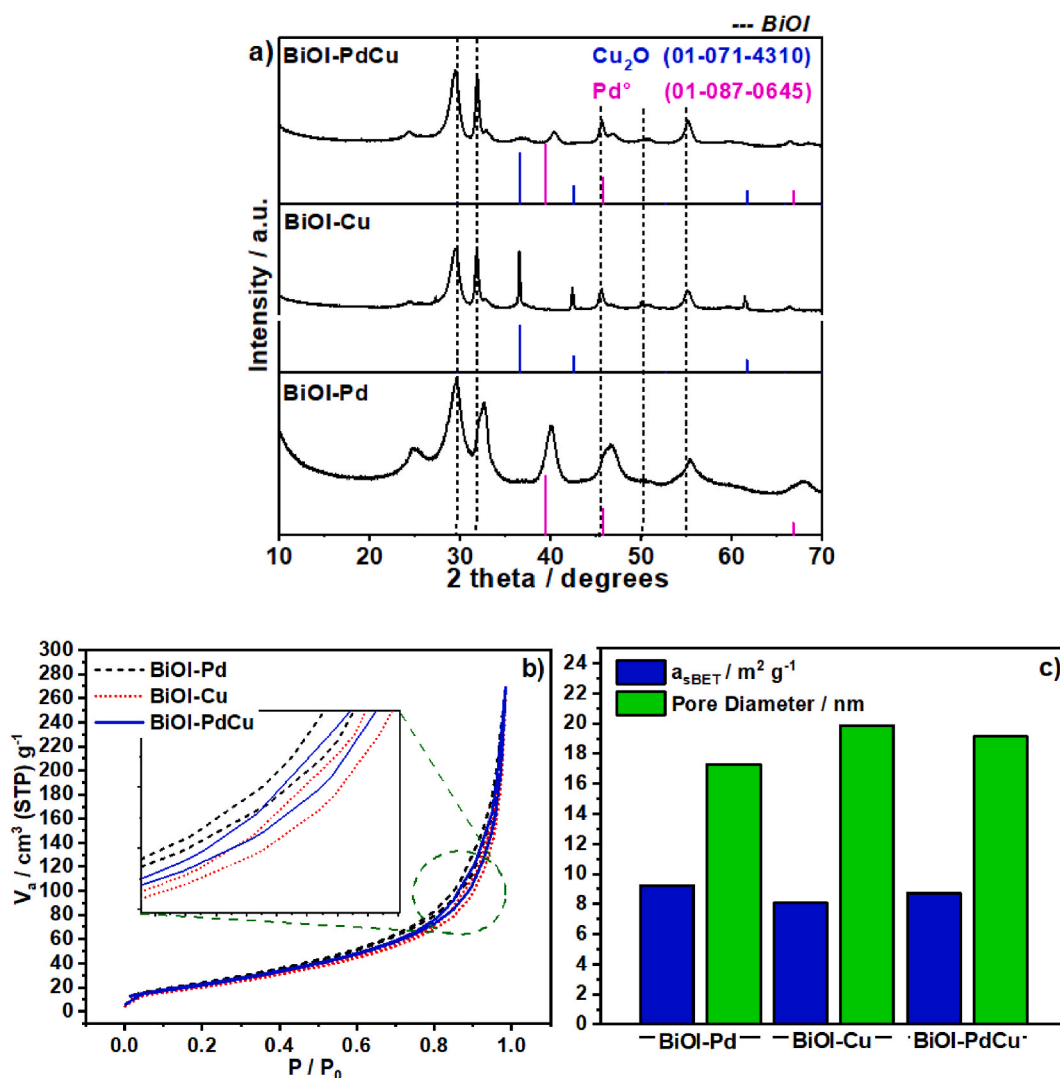
Fig. 5. a) XRD measurements, b) adsorption-desorption isotherms, and c) BET area and pore diameter estimations for BiOI-M (M = Pd, Cu, PdCu).

the CVs for Cu and PdCu NP's, respectively; since Cu is covered naturally for oxide species [52], both samples present a higher current under reduction potential when the samples are irradiated under N_2 saturated conditions. Under CO_2 saturation in dark conditions, the current below -0.8 V vs. RHE increases due to CO_2 electroreduction. As occurred in Pd NPs, the light irradiation induces an enhancement of the CO_2 conversion through a PEC process.

According to XRD and previous XPS measurements (Fig. S3), Cu^{1+} and Cu^{2+} are the main species in Cu and PdCu samples, respectively. However, the oxidized copper species are electrochemically reduced to Cu° previous to their interaction with the CO_2 molecule; Fig. S4 shows the comparison of cyclic voltammetry for Pd, Cu, and PdCu NPs. It is possible to observe that during the cathodic polarization, prior to the H_2 generation, all the samples present reduction signals attributed to the conversion of oxidized species to metal nanoparticles (-0.2 to 0.8 V vs. RHE), thus indicating that CO_2 interaction is carried out onto the metallic nanoparticles.

Regarding the composites BiOI–Pd, BiOI–Cu, and BiOI–PdCu (Fig. 6b, d, and 6f, respectively), it is evident that all samples show the same trend according to the experimental conditions; the current increases in the reduction region below -0.6 V vs. RHE as follows: N_2 saturated-dark $< N_2$ saturated-irradiated $< CO_2$ saturated-dark $< CO_2$ saturated-irradiated, thus corroborating PEC reactions is the most accurate process to improve the CO_2 reduction.

Finally, to determine the resulting CO_2 reduction products, a photocatalytic evaluation was performed for BIOI-Pd-Cu. These results are summarized in Fig. 7, where formic acid and acetic acid were detected in the measured liquid media, increasing their accumulation over time. Formic acid was the main product detected, accumulating 0.42 µmol g^{-1} after 3 h. The acetic acid accumulated 0.18 µmolg^{-1}. According to the literature, BiOI exhibits a conduction band potential of -1.1 V vs. NHE at pH 7 [53], favorable to reduce CO_2 to HCOOH (-0.12 V vs. NHE), and CH_3COOH (0.11 V vs. NHE) [54]. On the other hand, as observed in PEC
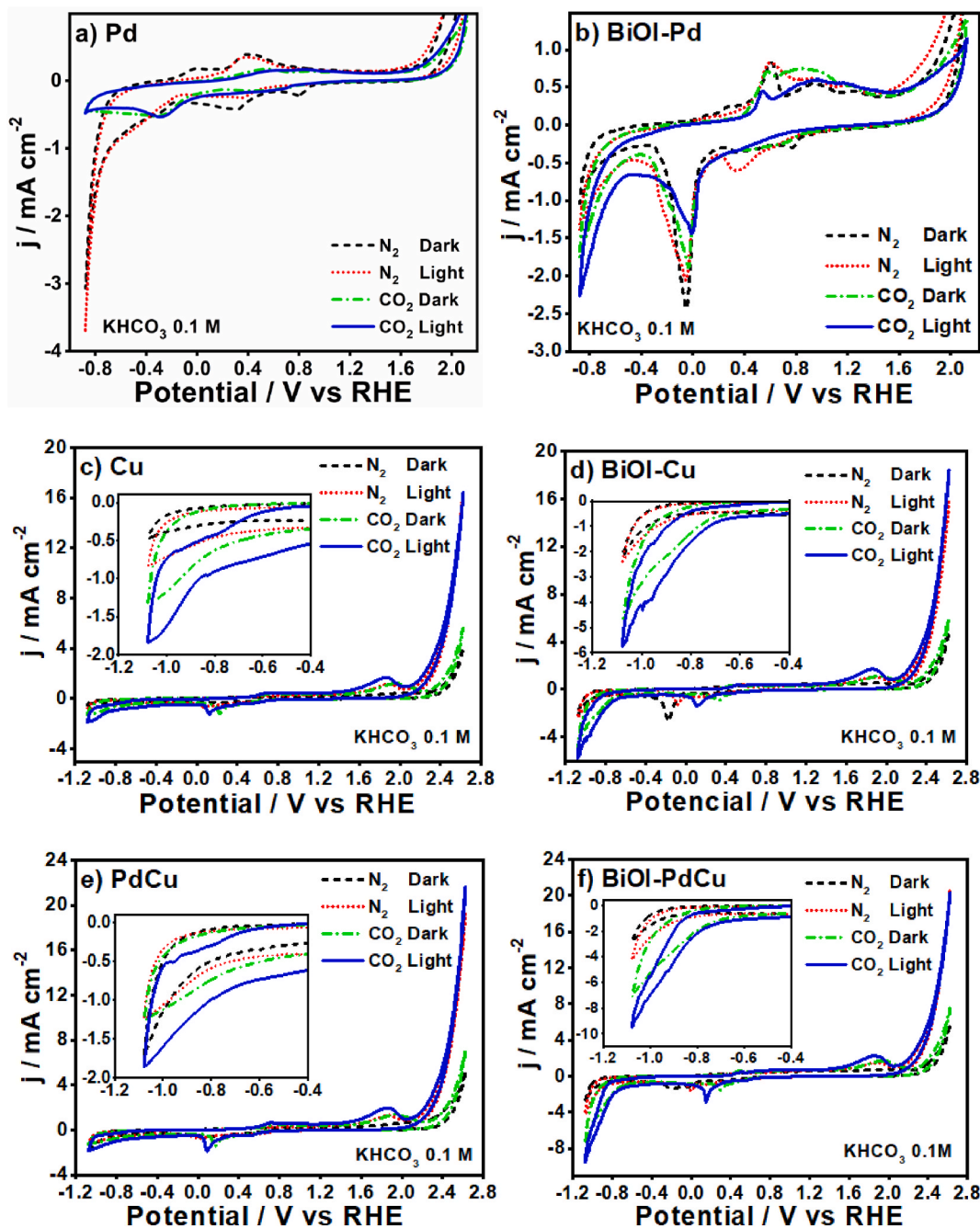
Fig. 6. Photoelectrochemical CO_2 reduction onto a) Pd, b) BiOI–Pd, c) Cu, d) BiOI–Cu, e) PdCu, and f) BiOI–PdCu.

measurements, the incorporation of Pd and Cu nanoparticles enhances the PEC activity promoting the affinity to adsorb CO_2 to convert it into value-added chemicals.

4. Conclusions

BiOX (X = Cl, Br, I) were successfully synthesized through a low-temperature hydrothermal method (160 °C). The three photo-catalysts present a p-type semiconductor behavior. BiOI showed the narrowest bandgap (1.9 eV) and the highest surface area and pore diameter compared to BiOCl and BiOBr. Additionally, BiOI showed the lowest charge transfer resistance. Such physicochemical and optical features are responsible for enhanced photocatalytic and photoelectrocatalytic activity to perform the CO_2 reduction reaction. Since BiOI was the most active photocatalyst, metallic NP's (Pd, Cu, PdCu) were used to fabricate the composites BiOI-M (M = Pd, Cu,
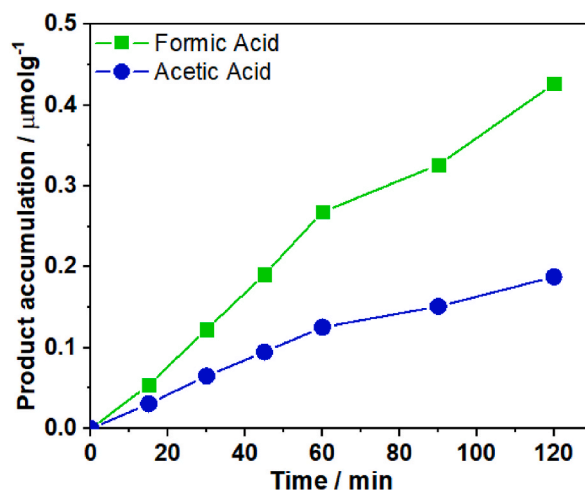
Fig. 7. Accumulation of carboxylic acids evolved from the photocatalytic CO_2 reduction onto the BiOI–PdCu photocatalyst.

PdCu). BiOI–PdCu showed a surface area increment compared to bare BiOI. The photoelectrocatalytic tests showed that incorporating Pd and Cu NP's onto BiOI increases the CO_2 reduction activity. BiOI–PdCu presented the highest density current at reduction potentials indicating an enhancement in the photoelectrocatalytic CO_2 reduction. Finally, BiOI–PdCu also presented activity in photoactivity in CO_2 reduction evolving formic acid and acetic acid under visible-light irradiation.

Author contribution statement

J.Manuel Mora-Hernandez: Conceived and designed the experiments; Performed the experiments; Analyzed and interpreted the data; Wrote the paper.

Luis A. Alfonso Herrera: Analyzed and interpreted the data; Wrote the paper.

Luis F. Garay-Rodriguez: Performed the experiments; Analyzed and interpreted the data; Wrote the paper.

Leticia M. Torres-Martínez: Contributed reagents, materials, analysis tools or data.

Irina Hernandez-Perez: Performed the experiments; Analyzed and interpreted the data; Contributed reagents, materials, analysis tools or data.

Data availability statement

Data will be made available on request.

Declaration of competing interest

The authors declare that they have no known competing financial interests or personal relationships that could have appeared to influence the work reported in this paper.

Acknowledgments

Appendix A. Supplementary data

Supplementary data to this article can be found online at https://doi.org/10.1016/j.heliyon.2023.e20605.

References

[1] A.R.B. Soutter, R. Mõttus, Global warming" versus "climate change": A replication on the association between political self-identification, question wording, and environmental beliefs. Journal of Environmental Psychology 69 (2020), 101413.

[2] X. Wang, D. Jiang, X. Lang, Future extreme climate changes linked to global warming intensity, Sci. Bull. 62 (24) (2017) 1673–1680.

[3] G.P. Peters, Carbon footprints and embodied carbon at multiple scales, Curr. Opin. Environ. Sustain. 2 (4) (2010) 245–250.

[4] J. Liang, 1 - chemical composition of the atmosphere of the Earth, in: J. Liang (Ed.), Chemical Modeling for Air Resources, Academic Press, Boston, 2013, pp. 3–20.

[5] T.R. Anderson, E. Hawkins, P.D. Jones, CO2, the greenhouse effect and global warming: from the pioneering work of Arrhenius and Callendar to today's Earth System Models, Endeavour 40 (3) (2016) 178–187.

[6] D.J. Easterbrook, Chapter 9 - greenhouse gases, in: D.J. Easterbrook (Ed.), Evidence-Based Climate Science, second ed., Elsevier, 2016, pp. 163–173.

[7] H.S. Whang, et al., Heterogeneous catalysts for catalytic CO2 conversion into value-added chemicals, BMC Chemical Engineering 1 (1) (2019) 9.

[8] D. Pandey, M. Agrawal, J.S. Pandey, Carbon footprint: current methods of estimation, Environ. Monit. Assess. 178 (1) (2011) 135–160.

[9] J. Rogelj, et al., Energy system transformations for limiting end-of-century warming to below 1.5 °C, Nat. Clim. Change 5 (6) (2015) 519–527.

[10] T. Daim, et al., Technology assessment for clean energy technologies: the case of the Pacific Northwest, Technol. Soc. 31 (3) (2009) 232–243.

[11] T.-S. Chung, et al., Emerging forward osmosis (FO) technologies and challenges ahead for clean water and clean energy applications, Current Opinion in Chemical Engineering 1 (3) (2012) 246–257.

[12] K. Habib, H. Wenzel, Exploring rare earths supply constraints for the emerging clean energy technologies and the role of recycling, J. Clean. Prod. 84 (2014) 348–359.

[13] G. Liu, et al., Manipulating intermediates at the Au–TiO2 interface over InP nanopillar array for photoelectrochemical CO2 reduction, ACS Catal. 11 (18) (2021) 11416–11428.

[14] I. Merino-Garcia, et al., Efficient photoelectrochemical conversion of CO2 to ethylene and methanol using a Cu cathode and TiO2 nanoparticles synthesized in supercritical medium as photoanode, J. Environ. Chem. Eng. 10 (3) (2022), 107441.

[15] C. Li, et al., Construction of heterostructured Sn/TiO2/Si photocathode for efficient photoelectrochemical CO2 reduction, ChemSusChem 15 (8) (2022), e202200188.

[16] Q. Wang, et al., Graphene oxide wrapped CH3NH3PbBr3 perovskite quantum dots hybrid for photoelectrochemical CO2 reduction in organic solvents, Appl. Surf. Sci. 465 (2019) 607–613.

[17] B. Wang, et al., Cu@porphyrin-COFs nanorods for efficiently photoelectrocatalytic reduction of CO2, Chem. Eng. J. 396 (2020), 125255.

[18] K. Xu, et al., In situ cofactor regeneration enables selective CO2 reduction in a stable and efficient enzymatic photoelectrochemical cell, Appl. Catal. B Environ. 296 (2021), 120349.

[19] S. Zhou, et al., Accelerating electron-transfer and tuning product selectivity through surficial vacancy engineering on CZTS/CdS for photoelectrochemical CO2 reduction, Small 17 (31) (2021), 2100496.

[20] S. Ren, et al., Excellent performance of the photoelectrocatalytic CO2 reduction to formate by Bi2S3/ZIF-8 composite, Appl. Surf. Sci. 579 (2022), 152206.

[21] Y. Yang, et al., BiOX (X = Cl, Br, I) photocatalytic nanomaterials: applications for fuels and environmental management, Adv. Colloid Interface Sci. 254 (2018) 76–93.

[22] L. Zhao, et al., First-principles study on the structural, electronic and optical properties of BiOX (X=Cl, Br, I) crystals, Phys. B Condens. Matter 407 (17) (2012) 3364–3370.

[23] C. Chuaicham, et al., Fabrication and characterization of ternary sepiolite/g-C3N4/Pd composites for improvement of photocatalytic degradation of ciprofloxacin under visible light irradiation, J. Colloid Interface Sci. 577 (2020) 397–405.

[24] X. Meng, Z. Li, Z. Zhang, Palladium nanoparticles and rGO co-modified BiVO4 with greatly improved visible light-induced photocatalytic activity, Chemosphere 198 (2018) 1–12.

[25] X. Meng, et al., Enhanced visible light-induced photocatalytic activity of surface-modified BiOBr with Pd nanoparticles, Appl. Surf. Sci. 433 (2018) 76–87.

[26] D. Ramírez-Ortega, et al., Effect of Pd and Cu co-catalyst on the charge carrier trapping, recombination and transfer during photocatalytic hydrogen evolution over WO3–TiO2 heterojunction, J. Mater. Sci. 55 (35) (2020) 16641–16658.

[27] C. Zhang, L. Zhou, J. Peng, Blue-light photoelectrochemical aptasensor for kanamycin based on synergistic strategy by Schottky junction and sensitization, Sensor. Actuator. B Chem. 340 (2021), 129898.

[28] K.N. Nishinohara Ippei, Maruoka Hirokazu, Hirai Shoji, H. Eba, Powder X-ray diffraction analysis of lime-phase solid solution in converter slag, ISIJ Int. 55 (3) (2015) 616–622.

[29] V.V.V. Stanev Valentin, A. Gilad Kusne, Antoszewski Graham, Ichiro Takeuchi, S. Alexandrov Boian, Unsupervised phase mapping of X-ray diffraction data by nonnegative matrix factorization integrated with custom clustering, npj Comput. Mater. 4 (1) (2018) 43.

[30] G.V. Raynor, The lattice spacings of substitutional solid solutions, Trans. Faraday Soc. 45 (0) (1949) 698–708.

[31] C.S. Wang Shubin, Yiwang Jia, Zhi Hu, Baode Sun, FCC-L12 ordering transformation in equimolar FeCoNiV multi-principal element alloy, Mater. Des. 168 (2019), 107648.

[32] H.-F.A.M. Soto-Arreola Aurora, J.M. Mora-Hernández, M. Torres-Martínez Leticia, *Improved photocatalytic activity for water splitting over MFe2O4–ZnO (M = Cu and Ni) type-ll heterostructures*, J. Photochem. Photobiol. Chem. 364 (2018) 433–442.

[33] J.N. Kondo, K. Domen, Crystallization of mesoporous metal oxides, Chem. Mater. 20 (3) (2008) 835–847.

[34] M. Coto, et al., Optimization of the microstructure of TiO2 photocatalytic surfaces created by Plasma Electrolytic Oxidation of titanium substrates, Surf. Coating. Technol. 411 (2021), 127000.

[35] J.M. Mora-Hernandez, et al., A comparative differential electrochemical mass spectrometry (DEMS) study towards the CO2 reduction on Pd, Cu, and Sn -based electrocatalyst, J. CO2 Util. 47 (2021) 101504.

[36] E.A. Davis, N.F. Mott, Conduction in non-crystalline systems V. Conductivity, optical absorption and photoconductivity in amorphous semiconductors, Phil. Mag.: A Journal of Theoretical Experimental and Applied Physics 22 (179) (1970) 903–922.

[37] D.L. Wood, J. Tauc, Weak absorption tails in amorphous semiconductors, Phys. Rev. B 5 (8) (1972) 3144–3151.

[38] Z. Chen, et al., UV-vis spectroscopy, in: Z. Chen, H.N. Dinh, E. Miller (Eds.), Photoelectrochemical Water Splitting: Standards, Experimental Methods, and Protocols, Springer New York, New York, NY, 2013, pp. 49–62.

[39] J. Hou, et al., Micro and nano hierachical structures of BiOI/activated carbon for efficient visible-light-photocatalytic reactions, Sci. Rep. 7 (1) (2017), 11665.

[40] C. Hua, et al., Synthesis of a BiOCl1−xBrx@AgBr heterostructure with enhanced photocatalytic activity under visible light, RSC Adv. 8 (30) (2018) 16513–16520.

[41] Y.-M. Xia, et al., Peony-like magnetic graphene oxide/Fe3O4/BiOI nanoflower as a novel photocatalyst for enhanced photocatalytic degradation of Rhodamine B and Methylene blue dyes, J. Mater. Sci. Mater. Electron. 31 (3) (2020) 1996–2009.

[42] C. Zhao, et al., BiOBr/BiOCl/carbon quantum dot microspheres with superior visible light-driven photocatalysis, RSC Adv. 7 (83) (2017) 52614–52620.

[43] M. Thommes, et al., Physisorption of gases, with special reference to the evaluation of surface area and pore size distribution (IUPAC Technical Report) 87 (9–10) (2015) 1051–1069.

[44] M. Hojamberdiev, et al., Unraveling the photoelectrochemical behavior of Ni-modified ZnO and TiO2 thin films fabricated by RF magnetron sputtering, J. Electroanal. Chem. 882 (2021), 115009.

[45] D. Guerrero-Araque, et al., SnO2–TiO2 structures and the effect of CuO, CoO metal oxide on photocatalytic hydrogen production, J. Chem. Technol. Biotechnol. 92 (7) (2017) 1531–1539.

[46] R. Qian, et al., Charge carrier trapping, recombination and transfer during TiO2 photocatalysis: an overview, Catal. Today 335 (2019) 78–90.

[47] L.M. Peter, et al., Interpretation of photocurrent transients at semiconductor electrodes: effects of band-edge unpinning, J. Electroanal. Chem. 872 (2020), 114234.

[48] A. Annamalai, et al., Sn/Be sequentially co-doped hematite photoanodes for enhanced photoelectrochemical water oxidation: effect of Be2+ as co-dopant, Sci. Rep. 6 (1) (2016), 23183.

[49] H.K. Dunn, et al., Tin doping speeds up hole transfer during light-driven water oxidation at hematite photoanodes, Phys. Chem. Chem. Phys. 16 (44) (2014) 24610–24620.

[50] E. Van Gheem, et al., Electrochemical impedance spectroscopy in the presence of non-linear distortions and non-stationary behaviour: Part I: theory and validation, Electrochim. Acta 49 (26) (2004) 4753–4762.

[51] E. Nouri, M.R. Mohammadi, P. Lianos, Construction of perovskite solar cells using inorganic hole-extracting components, ACS Omega 3 (1) (2018) 46–54.

[52] J. Li, et al., Investigations on the effect of Cu^{2+}/Cu^{1+} redox couples and oxygen vacancies on photocatalytic activity of treated $LaNi_{1-x}Cu_xO_3$ (x=0.1, 0.4, 0.5), Int. J. Hydrogen Energy 35 (23) (2010) 12733–12740.

[53] G.-J. Lee, Y.-C. Zheng, J.J. Wu, Fabrication of hierarchical bismuth oxyhalides (BiOX, X=Cl, Br, I) materials and application of photocatalytic hydrogen production from water splitting, Catal. Today 307 (2018) 197–204.

[54] J. Albero, Y. Peng, H. García, Photocatalytic CO_2 reduction to C2+ products, ACS Catal. 10 (10) (2020) 5734–5749.